Proceedings of the 21st ICSMGE, Vienna, Austria, 14 – 19 June 2026. Pistrol, Adam & Schweiger (eds.)
Published by: ÖGG, Austrian Society for Geomechanics, Salzburg, Austria, ISBN 978-3-9503898-4-5
https://doi.org/10.53243/ICSMGE2026-813

Permanent displacement of full height rigid facia geosynthetic reinforced soil walls for high-speed railway corridors

Suman Haldar, Debayan Bhattacharya, Bappaditya Manna
Civil & Environmental Engineering, Indian Institute of Technology, Delhi, New Delhi, 110016, India, cez228138@iitd.ac.in

ABSTRACT: Design of critical infrastructure like full height rigid (FHR) facia Geosynthetic Reinforced Soil (GRS) walls for High-Speed Railway (HSR) corridors are now-a-days shifting from force-based to performance-based approach. In the Indian subcontinent's context, the HSR is being developed with a goal of train speed reaching greater than 300 kmph on state-of-the-art dedicated corridors. Site-specific performance-based design of GRS walls under seismic load conditions calls for special attention. This study proposes an analytical framework for an experimentally observed double-wedge rupture plane often reported in the case of GRS walls subjected to earthquake excitation. Critical yield acceleration has been evaluated every instant, considering the actual acceleration time history. Computed wall displacements from the critical yield acceleration time history have been verified against existing numerical and laboratory studies for the efficacy of the proposed analytical framework in this study. This investigation also provides insights into the dependency of maximum geosynthetic reinforcement demand on critical yield acceleration. Permanent displacement estimates for FHR-GRS walls based on Bhuj (2001) earthquake scaled to site-specific probable range of Peak Ground Acceleration (PGA) have been expressed as a function of friction-angle of the backfill (ϕ'), unit weight of backfill (γ), and primary reinforcement length (L) to wall height (H) ratio as well as equivalent surcharge corresponding to HSR travelling with a speed range greater than 300 kmph.

KEYWORDS: Geosynthetics, Retaining Wall, Performance-Based Design, Permanent Displacement, High-Speed Railway.

1 INTRODUCTION

Geosynthetic Reinforced Soil (GRS) structures have become increasingly prevalent in civil engineering due to their cost-effectiveness, rapid construction, and superior tolerance to differential settlement. These structures are widely adopted on roadways, bridge abutments, and railway embankments, offering enhanced seismic resilience, durability and sustainability compared to traditional retaining walls (Bathurst & Hatami, 1998; Hatami & Bathurst, 2006; Tatsuoka, 2021). Despite the extensive use of GRS walls in various infrastructure projects, the application in High-Speed Railway (HSR) systems often remains limited. As HSR networks expand globally, understanding the performance and advantages of GRS walls under dynamic loading conditions is critical for advancing resilient and sustainable transportation infrastructure.

Back-to-back Mechanically Stabilized Earth Walls (BBMSEWs) are a type of GRS wall that offers reduced carbon footprint, enhanced stability, and improved aesthetics, and have gained popularity in the transportation sector worldwide. Federal Highway Administration (Berg, et al., 2009) highlighted the BBMSEW as independent and interactive dependent walls based on the non-overlapping and overlapping of the active thrusts of two walls under static loading and earthquake acceleration of less than 0.05g (Berg, et al., 2009). Effects of surcharge, load uncertainty and seismic impacts on BBMSEW are missing in various international guidelines & standards of GRS walls (Berg, et al., 2009; BS 8006, 2010; IRC: SP: 102, 2014; IS 18591, 2024). However, published literature (Kamalzadeh & Pender, 2023) emphasizes several crucial elements of backfill and reinforcement in the design of BBMSEW under earthquake loading and for their inclusion in various guidelines.

Helwany, et al. (1996) illustrated the functions of flexible facia, like wrapped around, and rigid facia, like segmental modular brick, precast panel facing, wrapped around in-situ full height rigid (FHR) facia in GRS walls. FHR facing provides superior stability than conventional facia, mobilizing higher lateral thrust for extreme events like earthquakes, tsunamis and excessive vibration caused by high-speed trains.

The influence of surcharge loading on GRS walls has been shown to significantly affect structural design parameters such as lateral stress, overall stability, and reinforcement strength distribution, as extensively documented in prior research (Hatami & Bathurst, 2006; Sravanam, et al., 2019). Dynamic responses due to HSR passages on MSE walls are studied to some extent through static surcharge and cyclic (Joseph & Banerjee, 2025). Tatsuoka (2021) stated an Equation (1) to obtain static surcharge q_t due to rail track far away from wall. Repetitive loading due to train passage can also be implemented through the dynamic amplification factor, α, calculated using the American Railroad Engineering Association (AREA) formulation equation (2) proposed by (Prause, 1974).

$$q_t = P_{axle}/d_{axle}.B_0 \quad (1)$$

$$\alpha = 5.21.V/D_{wheel} \quad (2)$$

Where, P_{axle} is Axle load in kN, d_{axle} = Distance between axles in m, B_0 = Train load distribution width in m, V = vehicle speed in km/h, and D_{wheel} = wheel diameter in mm.

A worldwide shift of design convention from traditional pseudo-static limit-equilibrium methods to Performance-Based Design (PBD) for GRS walls (Koseki, et al., 1998) is driven by the inability of traditional safety factors to adequately evaluate seismic performance and the post-earthquake residual state of the structure. Insights on permanent displacement evaluation of GRS walls from PBD (Gaudio, et al., 2018; Horii, et al., 1994) laid the stepping-stone for site-specific displacement-based design charts. Glimpses of these aspects can be found in studies related to cantilever retaining walls as well by (Jadhav & Prashant, 2019). Previous PBD charts of GRS wall (Gaudio, et al., 2018) overpredict considering plastic mechanism, leading to uneconomical design aspects. The present study proposes an analytical framework for a double wedge failure plane reported for an independent BBMSEW defined by the distance between two walls, $W_{wall} \geq 1.13$ of wall height, H, following (Siddharthan, et al., 2004) with FHR facia, aims to provide more reliable and convenient site-specific PBD charts for GRS walls subjected to HSR passages and seismic loading.

2 DOUBLE WEDGE METHOD & VALIDATION

2.1 *Failure Mechanism & Motivation*

Kinematic failure mechanism of GRS wall has been analyzed using various approaches like force stabilization (Berg, et al., 2009), acceleration compatibility (Horii, et al., 1994), energy conservation (Gaudio, et al., 2018) on single wedge using log-

spiral and planar surface or double wedge failure plane. Berg et al. (2009) considered failure planes of independent BBMSEWs that pass through the bottom of reinforced soil (locked soil mass), following an outer rupture plane propagation at an angle of 45°+$\phi'/2$ within retained soil (soil wedge). However, Horii et al. (1994) introduced two-block mechanism in which both wedges subtend an angle with respect to the bottom surface of the GRS wall under base acceleration, based on observations of laboratory experiments (Koseki, et al., 1998; Bathurst & Hatami, 1998; Yazdandoust, et al., 2023), and numerical studies (Kamalzadeh & Pender, 2023), which have been implemented in the present study (Figure 1a).

2.2 *Analytical Framework Development*

An analytical framework has been established in the present study considering a BBMSEW, characterized by its straight wall height (H), holding back a uniform horizontal reinforced & retained backfill of cohesionless soil with unit weight (γ) and friction angle (ϕ') and reinforcement with ultimate tensile strength, (T_{ULT} *or* T) of uniform length L_1 or L, supported by a firm, non-deformable soil layer beneath the structure. The following assumptions are being made for the development of this analytical framework:

- Non-overlapping BBMSEW with $W_{wall} \geq 1.13H$
- A rigid-plastic Coulomb's failure wedge assuming uniform acceleration across the entire soil mass.
- Interaction between the soil-wall interface and the pad foundation is disregarded.
- Ground motion originates at the base of the wall.
- Soil wedge moves tangentially along the established rupture planes rather than perpendicular to the planes.
- As rigid base soil prevents downward movement of the wall, the vertical yield acceleration of the wall aligns with the vertical component of the ground acceleration.
- Kinematics of soil wedge results in wall displacement as a combination of rotation and translation.

The failure plane extends from the bottom wall towards the end of the locked mass, followed by the end of the retained soil of length L_2, termed as the outer, AB and inner rupture plane, BC, respectively (see Figure 1b). OB and BC subtend angles θ_1, and θ_2, with respect to the horizontal respectively. The yield acceleration components for the soil wedge are denoted as k_{hy}' and k_{vy}', and for the wall with locked soil mass as k_{hy}'' and k_{vy}'' under base acceleration of horizontal and vertical components k_h, k_v, as illustrated in Figure 1b. Assuming the structure to maintain equilibrium during earthquake excitation, resisting forces P_1 and R_N develop on the rupture planes of retained backfill, while tensile force T and resisting force R_F act on the rupture planes of reinforced backfill (Figure 1c). Referring to free body diagrams (Figure 1d) of double wedges, expression for the k_{hy}'' (3), with a factor of safety of 1, can be elucidated considering the force equilibrium of two wedges and acceleration compatibility at failure planes.

$$k_{hy}'' = \frac{R + WJ(1-k_v)D_1 + TJD_2}{1 + WJD_2} \quad (3)$$

Here,

$R = (\sin\theta_2 - \cos\theta_2 \tan\phi')(k_v \cos\theta_2 + k_h \sin\theta_2 - \cos\theta_2);$

$V = \sin(\theta_2 - \phi')\tan\phi' - \cos(\theta_2 - \phi');$

$D_1 = \tan\phi' \cos\theta_1 - \sin\theta_1;$

$D_2 = \cos\theta_1 + \sin\theta_1 \tan\phi';$

$J = \frac{V \cos\theta_2}{W_s[\tan\phi' \sin(\theta_1 - \phi') - \cos(\theta_1 - \phi')]}$

Value of θ_1, and θ_2 can be calculated using Coulomb's force triangle method for a specific L_2, aiming to maximize the active earth pressure force P_1 on the locked soil mass (Equations (4) & (5)). W_s & W represent the equilibrium weight of the soil wedge and locked soil mass, along with the self-weight of the wall, respectively. The angles formed by vectors R_N, P_1, and W_s are presented below.

$$P_1 = \frac{W_s \sin\tau}{\sin\mu} \quad (4)$$

Here, $\tau = \theta_2 - \phi' + \alpha; \nu = 90° - (\phi' + \alpha);$

$\mu = 180° - (\tau + \nu); \alpha = \tan^{-1}\left(\frac{k_{hy}''}{1 - k_{vy}''}\right);$

$$P_1 = \frac{(W+T)\sin\eta_2}{\sin\zeta} \quad (5)$$

Here, $\xi_1 = \tan^{-1}\left(\frac{T}{W+T}\right); \xi_2 = \tan^{-1}\left(\frac{W}{W+T}\right); \eta_1 = 90° + \phi' - \xi_1; \eta_2 = 90° - \theta_1 - \xi_2; \zeta = 90° - (\phi' - \theta_1);$

The equilibrium equation (6) formed due to the double wedge geometry is stated below.

$$H - L_1 \tan\theta_1 = L_2 \tan\theta_2 \quad (6)$$

For each distinct set of soil and reinforcement properties—including wall height (H), uniform geogrid length (L_1), friction angle (ϕ'), soil unit weight (γ), geogrid tensile strength (T), and seismic coefficient (k_h, k_v)—the critical wedge angles θ_1 & θ_2 are computed iteratively. The process begins by solving the geometric equilibrium (Equation (6)) and the force equilibrium conditions (Eqns. (4) & (5) for P_1, with initial α set to zero) to estimate θ_1 & θ_2. These angles are then used to evaluate k_{hy}'' via eqn. (3), after which the parameter α is updated and the process is repeated until successive θ_1 & θ_2 values converge within one degree. For each admissible L_2, the minimum k_{hy}'' is observed, representing the critical internal yield acceleration coefficient, $k_{hy,c}^{int''}$ for that design scenario. Permanent displacement of wall is calculated through double numerical integration when the earthquake acceleration surpasses the wall's yield acceleration, as stated in Newmark's sliding block method (Newmark, 1965).

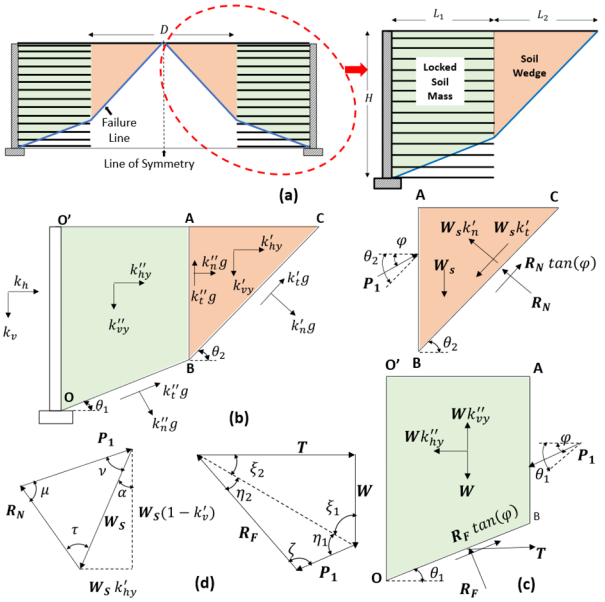

Figure 1. Analytical framework for Double Wedge method (a) Double wedge failure plane for independent BBMSEWs; (b) Acceleration acted along inner and outer rupture plane of double wedge; (c) Free body diagram of reinforced backfill and retained soil; (d) Force polygon for individual wedge.

2.3 *Benchmarking of the proposed framework*

The analytical approach for the two-wedge model is validated with one numerical simulation by Kamalzadeh & Pender, (2023) and one experimental investigation by Koseki, et al., (1998). These two studies considered mechanically stabilized

earth walls and analyzed the distinct features like acceleration at the reinforcement, active earth pressure variation over height and wall displacement. These studies considered uniform geogrid reinforcement on one side of the wall, which inherently depicts that the ends of the geogrid of the two walls are far apart. The permanent wall displacement, d_{perm}, obtained from the analytical approach adopted in this study is compared against the obtained values from literature (Table 1). Koseki, et al., (1998) also analyzed the double-wedge model analytically based on the methodology given by Horii et al. (1994). The critical internal yield acceleration coefficient values, $k_{hy,c}^{int"}$ and failure angle θ_2, from this study are also checked against those reported by Koseki et al. (1998). The present approach underpredicts the one reported by Kamalzedah and Pender (2023), where a two-surface plasticity model with a non-associated flow rule constitutive model was considered. However, a variation of 5–10% of the obtained results compared to these two studies indicates the reliability of the present analytical framework developed in this investigation.

Table 1. Summary of validation of the proposed analytical framework with published literature

Case Study	Parameters	Reported Values	Present Study
1. Numerical Study (Kamalzadeh & Pender, 2023) [H-8m, L- 4m, γ- 19.3 kN/m^3, ϕ'- 31.2°, Chichi EQ. (1999) HWA003, M_w 7.6, PGA 0.14g]	Permanent wall Displacement, d_{perm} (mm)	184	160
	Angle of the failure plane, θ_2	-	69°
	Critical Yield Acceleration, $k_{hy,c}^{int"}$ (g)	-	0.046
2. Experimental Study (Koseki et al., 1998) [H-0.5m, L- 0.2m, γ- 15.9 kN/m^3, ϕ'- 51°, horizontal sinusoidal load with frequency 5Hz for 140sec]	Permanent wall Displacement, d_{perm} (mm)	203	215
	Angle of the failure plane, θ_2	58°	59°
	Critical Yield Acceleration, $k_{hy,c}^{int"}$ (g)	0.529	0.502

3 PROBLEM STATEMENT

Design charts for permissible displacements for different soil and reinforcement demands under strong ground motions will lay the foundation for next-generation modelling and performance-based design of GRS structures around the world in the days to come. Site-specific displacement charts will further enhance the construction of complex earth structures, as illustrated by previous studies (Jadhav & Prashant, 2019; Kamalzadeh & Pender, 2023). Essential parameters required to develop site-specific displacement charts of GRS walls for HSR corridors are listed and elucidated in subsequent subsections.

Table 2. Adopted values of essential parameters of the GRS wall

Parameter	Values
Height of wall, H (m)	4, 6, 8
Length of Reinforcement/ Height of wall (L/H)	0.5, 0.7-1.0
Angle of friction of backfill, ϕ'	32°, 35°, 38°
Unit weight of backfill, γ (kN/m^3)	18, 20
Ultimate tensile strength of geogrid, T_{ULT} (kN/m)	20- 190
Vertical spacing between reinforcement, s_v (m)	0.3, 0.6

3.1 *Essential Parameters considered for GRS wall*

Reinforcement stiffness, spacing, length, and soil-reinforcement interaction primarily govern the deformation behaviour of the GRS wall (Bathurst & Hatami, 1998). Backfill material property, like angle of shearing resistance (ϕ'), soil unit weight (γ), influences the deformation mode of GRS walls (Bathurst & Hatami, 1998). International design guidelines and standards (Berg, et al., 2009; BS 8006, 2010; IRC: SP: 102, 2014; IS 18591, 2024) suggest a minimum L/H ratio of 0.7 and ϕ' values in the range of 30°- 40°. Woodruff (2003) observed a compound failure of GRS walls for a L/H ratio of 0.25-0.6. Strength demand is rarely affected by reinforcement spacing to wall height ratio (Michalowski, 1997). Parameters affecting the deformation behaviour of GRS walls are assumed in this study (Table 2) based on previous research reported by Gaudio et al (2018).

3.2 *Study Area*

In the context of the Indian subcontinent, the Indian Railways plans to build several high-speed rail projects, allowing for bullet train services with speeds greater than 300 kmph over a dedicated corridor connecting major cities to facilitate the vast transportation growth over the country. India's first-ever high-speed railway project, Mumbai-Ahmedabad High-Speed Railway (MAHSR), involves tunnels, bridges, overhead viaducts, and a special type of GRS walls like BBMSEW with FHR facia. Site-specific permanent displacement chart of such GRS walls will help in predicting deformation under severe seismic conditions and HSR loading. Based on a comprehensive soil database over the MAHSR stretch, it was observed that generally ML-SM soil followed by CI/CL soil up to a depth of 15m. Site based on the equivalent shear wave velocity of 30m, $V_{S,30}$ falls under class C and site class II as per Eurocode 8 and IS 1893: 2016, respectively.

The study area falls under seismic zone III to IV. The ground acceleration time history is estimated using DEEPSOIL v7.0, based on soil profile above bedrock and Bhuj (2001) earthquake motion (26/01/2001, M_w 7.7, PGA 0.1g, IITR station Ahmedabad), as obtained from COSMOS. Considering the overall seismic vulnerability of the study area, ground acceleration time history scaled to five maximum acceleration (k_{max}) levels of 0.1, 0.15, 0.2, 0.35, and 0.5g. Vertical acceleration coefficient, k_v is assumed as 0.5 times of horizontal acceleration, k_h. However, Gaudio et al (2018) observed a minor influence of k_v on permanent displacement of GRS wall.

3.3 *Static and Dynamic Surcharge*

Ballastless HSR slab track comprises of components above backfill and GRS wall with rigid facia (Joseph & Banerjee, 2025). Static surcharge includes the weight of the layers above the GRS wall and the axle load of the bullet train, which lies between 10.8-17 tons (Joseph & Banerjee, 2025). Static surcharge q_t is equated corresponding to 17 tons of axle load with distance between axles as 2.5 m, and load distribution width as 4.3 m (Equation (1)). Dynamic amplification factors (Equation (2)) for train speeds of 300, 320, 360, and 400 km/h with a wheel diameter of 910 mm are applied to static surcharge loads to determine the dynamic surcharge values that are further implemented in this investigation.

4 REINFORCEMENT STRENGTH DEMAND

The reinforcement strength demand in the performance-based design of GRS walls is a critical parameter as it governs the ability of the structure to accommodate seismic-induced deformations while ensuring stability under prescribed displacement limits. This strength demand is intrinsically linked to the critical yield acceleration, which represents the threshold seismic coefficient at which internal plastic mechanisms are activated, directly correlating the required reinforcement capacity to the wall's seismic performance objectives (Gaudio, et al., 2018).

Non-dimensional form of reinforced strength demand, $k_t/\gamma H$, expressed by Michalowski (1997), stated in Equation (7), is compared with $k_{hy,c}^{int"}$. This has been presented in Figure 2,

involving all considered essential parameters in this study (see Table 2).

$$k_t/\gamma\, H = T/s_v\, \gamma\, H. \quad (7)$$

The concave decremental nature of Figure 2 (a-f) indicates that at low reinforcement demands ($k_t/\gamma H$ <1.8), increasing reinforcement reduces the critical acceleration coefficient by 1.25 times before it starts to increase at higher reinforcement demands ($k_t/\gamma H \geq 1.8$). This behaviour highlights a non-linear relationship between geogrid reinforcement demand and seismic stability at low reinforcement levels ($k_t/\gamma H$ <1.8). The analysis reveals that with L/H=0.5 & for ϕ'=32° (Figure 2 a), a steeper reinforcement demand is observed (2.8< $k_t/\gamma H$ <5) with higher critical yield acceleration coefficients (0.25-1). It represents a transition from a compound failure mechanism to a steeper localized failure mode. The limited reinforcement length (L/H=0.5) cannot effectively anchor beyond the critical failure plane, resulting in a steep failure plane in reinforced soil mass to compensate for the reduced confinement effectiveness.

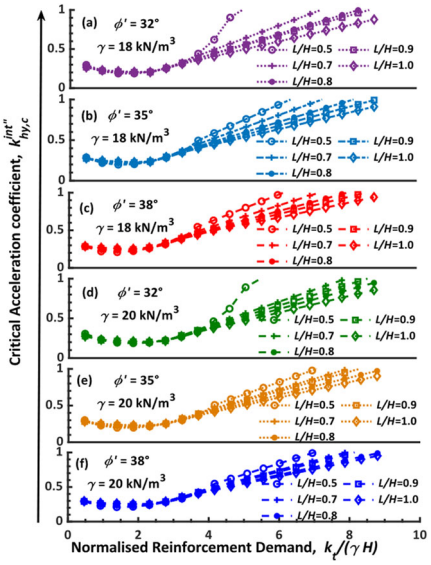

Figure 2. Parameter-based reinforcement strength demand curves.

As L/H increases (0.7-1), observed in Figure 2 a-f, the curves become flatter and spread over a wider region (2.8< $k_t/\gamma.H$ <9), indicating a more distributed failure mechanism. This is also accompanied by a reduced rate of increase in reinforcement demand (13.6%-16.7%) in comparison to L/H=0.5 (21.42%-50%) for a similar increase of yield acceleration, due to the greater effectiveness and engagement of longer reinforcements embedded within the soil mass. Variations in unit weight γ show minimal deviations (1-2%) in the nature of the strength demands, highlighting that γ has a secondary influence compared to ϕ' and wall geometry (L/H). Higher angle of internal friction (ϕ'=35°, 38°) tends to exhibit a flatter response for all L/H ratios, with shear strength estimates reduction rate of 18-21% as compared to ϕ'=32° (Figure 2 a-f). This phenomenon reflects the enhanced shear strength capacity of the backfill, which reduces the required reinforcement contribution to maintain the overall wall stability of the GRS structure.

5 SITE-SPECIFIC PERMANENT DISPLACEMENT ESTIMATE

Seismic loads exceeding the internal resistance of the GRS wall ($k_{hy,c}^{int"}$) lead to permanent displacement (d_{perm}), estimated by double integrating the relative acceleration following Newmark's sliding block method (Newmark, 1965). Conventional design charts developed, (Newmark, 1965; Richards & Elms, 1979; Cai & Bathurst, 1996; Whitman & Liao, 1985) remain fundamentally limited by their reliance on Newmark's rigid block analysis assumptions, which neglects realistic phenomena including dynamic backfill response, soil-structure interaction effects, failure surface inclination variations, and amplification characteristics that can significantly impact displacement predictions. A viable alternative involves employing a simplified analytical approach that utilizes parametric integration of regional synthesized earthquake motion, backfill response and critical failure surface, which are systematically investigated in this study.

Non-dimensional form of permanent displacement, d' (= $d_{perm}/[v_{max}^2/k_{max}\, g]$) of Site Class C as per Eurocode 8, are evaluated based on Newmark's sliding block analysis considering k_h, k_v, $k_{hy,c}^{int"}$ for static, dynamic and no surcharge case (Figure 3). They are compared against already existing literature on PBD of earth retaining walls (Newmark, 1965; Richards & Elms, 1979; Cai & Bathurst, 1996; Whitman & Liao, 1985; Gaudio, et al., 2018). v_{max} represents maximum peak velocity ($v_{max} = T_{v_c}/2\pi\, k_{max}\, g$). T_{v_c} is considered 0.25s for Site C, as it depicts the starting period of the constant velocity of the design spectrum in Eurocode 8. Three distinct acceleration ranges of $k_{hy,c}^{int"}/k_{max}$ (lower range: 0.1-0.3, middle range: 0.3-0.5, and higher range: 0.5-0.8) in Figure 3 reveal variations in prediction accuracy with classical charts reported earlier in existing literature. In the lower and middle range, the present study's predictions for no surcharge underpredict by 11-93% and 38-92% to most conventional methods (C1, C5, & C6), except for C3 & C4 (58-74% & 56-88%). It nearly matched with C2 with slight variations of 5-11%. It indicates a consistency with the fundamental sliding block principle but diverges from the upper-bound approaches. Overpredicted permanent displacements in lower and middle range based on upper bound approaches (C5 & C6) will lead to uneconomical design. Also, the present model at a higher range yields higher values than only Newmark's mean (C2) value by 61% but demonstrates lower predictions than all other studies, like C1-C2 & C4-C6 by 27-96%. This behaviour suggests that the current approach may underestimate the true seismic capacity of GRS walls at high acceleration levels (0.5-0.8) due to consideration of higher a_{max}, disregarding plastic mechanism, potentially leading to conservative designs at higher ranges.

The influence of surcharge loading on the critical yield acceleration curves demonstrates complex behaviour patterns across different acceleration ranges (lower, middle, and high ranges) (Figure 4 a). It presents two bar charts that analyze d_{perm} variation under static and dynamic surcharge conditions as a function of the normalized critical internal acceleration

Table 3. Coefficients to determine 95th percentile permanent displacement, d_{perm} (R^2 =0.9-0.95)

L/H	**SITE C (without surcharge)**			**SITE C (with static surcharge)**		
	a (m)	*b*	$k_{hy,c}^{int"}/k_{max}$	*a* (m)	*b*	$k_{hy,c}^{int"}/k_{max}$
0.5-1	0.609	7.261	0.1- 1	0.339	5.486	0.16- 1
0.7-1	4.112	10.18	0.32- 1	1.155	7.461	0.33- 1
L/H	**SITE C (with dynamic surcharge- 300Kmph)**			**SITE C (with dynamic surcharge- 320Kmph)**		
	a (m)	*b*	$k_{hy,c}^{int"}/k_{max}$	*a* (m)	*b*	$k_{hy,c}^{int"}/k_{max}$
0.5-1	0.425	5.108	0.24- 1	0.425	5.108	0.24- 1
0.7-1	3.975	9.921	0.35- 1	3.971	9.92	0.35- 1
L/H	**SITE C (with dynamic surcharge- 360Kmph)**			**SITE C (with dynamic surcharge- 400Kmph)**		
	a (m)	*b*	$k_{hy,c}^{int"}/k_{max}$	*a* (m)	*b*	$k_{hy,c}^{int"}/k_{max}$
0.5-1	0.425	5.1	0.24- 1	0.426	5.111	0.24- 1
0.7-1	3.989	9.931	0.35- 1	4.017	9.95	0.35- 1

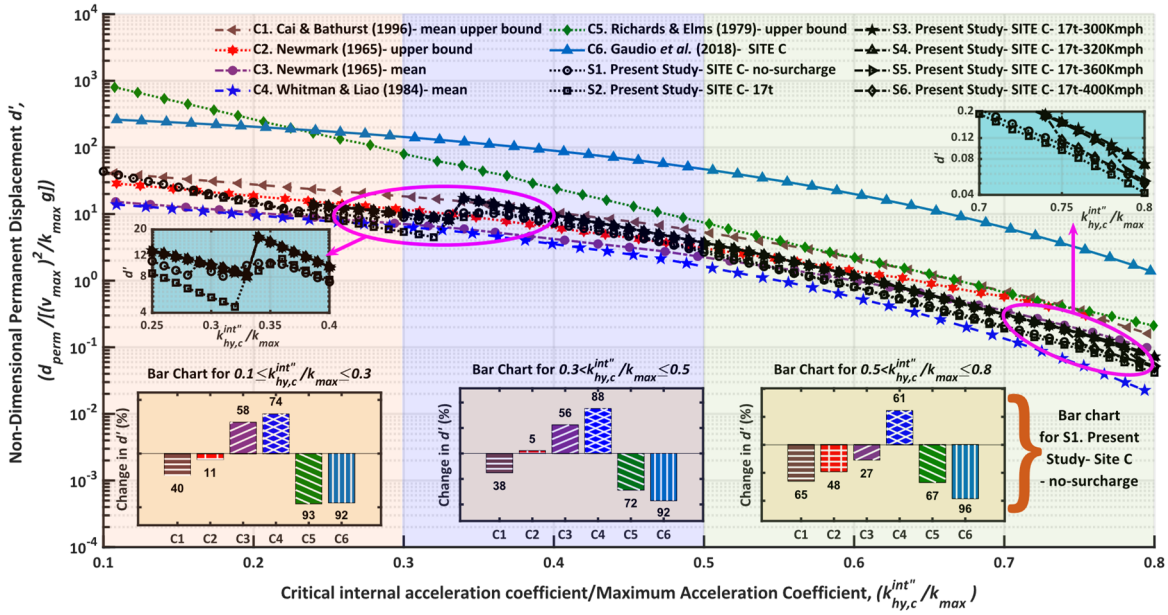

Figure 3. Comparison of non-dimensional permanent displacement with and without static and dynamic surcharge against published literature (C1-C6)

coefficient ($k_{hy,c}^{int"}/k_{max}$). Static surcharge with an axle load of 17 tonnes exhibits significant changes in d_{perm} compared to the no-surcharge condition (0.8-11% increase at mid-range, while 2-43% decrease at low and high range). A minimal influence on the mid-acceleration range is observed, whereas a significant impact on the fundamental wall stability characteristics at the low acceleration range is noticed. Notably, in the 0.23-0.33 range of normalized critical internal acceleration, static surcharge effects demonstrate lower values (2-43%) than no-surcharge condition. This phenomenon may be attributed to the beneficial mass effect stated in Kramer (1996), where additional weight enhances resistance to overturning moments at low and higher acceleration levels, while the inertial effects remain modest at intermediate acceleration ranges.

Interestingly, dynamic surcharge conditions consistently show higher values than both static surcharge (18-93%) and no-surcharge (18-66%) scenarios, reflecting the amplification effect of seismic loading on superimposed loads of almost 1.6-6 times (Figure 4 b). The effect is most pronounced (nearly 6 times) at intermediate acceleration in the case of high dynamic surcharge for a train speed of 400 km/h. Magnification effect also nullifies the inertial effects at low acceleration ranges, leading to a 47-93% increase in d_{perm} compared to static surcharge. Substantial increase in permanent displacement of GRS walls due to dynamic surcharges over all acceleration ranges highlights the necessity of accounting for performance-based design to overcome significant underestimation of wall displacements and potential serviceability issues.

It is imperative to point out that a sudden shift of d_{perm} in $k_{hy,c}^{int"}/k_{max}$ about 0.34 irrespective of surcharge type is due to the wall transitions from a compound failure mechanism to a localized or steeper failure mechanism. As the acceleration coefficient increases, the failure surface rapidly shifts, causing a sudden increase in the mobilized displacement (83-116%).

For wall geometry L/H<0.7, a significant part of reinforcement suddenly becomes ineffective, leading to a sharp increase in displacement because the remaining reinforcement cannot provide sufficient resistance. For longer reinforcements (L/H≥0.7), the reinforcement extends beyond the critical failure surface, maintaining effective anchorage as the failure mechanism evolves. This illustration indicates the reason why a minimum L/H= 0.7 is required for GRS walls to avoid failure mechanism shift, coherent with international guidelines (Berg, et al., 2009; BS 8006, 2010; IRC: SP: 102, 2014; IS 18591, 2024).

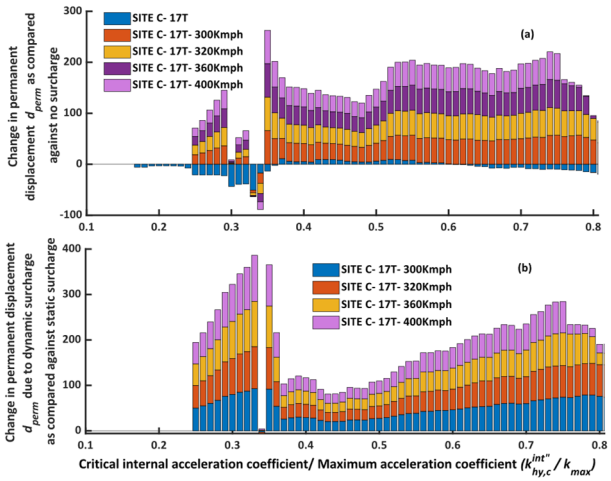

Figure 4. (a) Comparative change in permanent displacement of GRS wall due to the effect of static and dynamic surcharge with respect to the no-surcharge case, (b) Dynamic amplification effect on permanent displacement of GRS wall compared to static surcharge.

Rampello et al. (2010) proposed a decreasing exponential function of 95th upper-bound percentile permanent displacement, d_{perm} with $k_{hy,c}^{int"}/k_{max}$ (Equation (8)), which relatively captures the pattern observed for various cases (Figure 3).

$$d_{perm} = a.e^{-b.\frac{k_{hy,c}^{int"}}{k_{max}}}. \quad (8)$$

Here, a and b are the coefficients to determine the 95th percentile permanent displacement. Coefficients a & b of the Equation (8) for the present study, considering static, dynamic and no surcharge cases are summarized in Table 3. Coefficients are valid for the range of L/H and $k_{hy,c}^{int"}/k_{max}$ (see Table 3).

The design procedure for implementing the current analytical framework for GRS walls is below.

1. Consider allowable permanent displacement of GRS wall, regional a_{max}, Site Class, HSR speed, and evaluate $k_{hy,c}^{int"}$ using Figure 3 & Table 3.
2. Using equations of Appendix C from Gaudio et al. (2018), estimate minimum L/H to stabilize external failure mode.

3. Calculate $k_t/\gamma H$ following Figure 2 based on higher L/H than the minimum obtained in Step 2 & $k_{hy,c}^{int"}$ estimated in Step 1 for essential parameters like wall height, H, soil property, ϕ', and unit weight of soil, γ.
4. Calculate vertical reinforcement spacing, s_v and tensile strength, T, from equation (7). Customize s_v and T according to the needs of construction interest.

6 CONCLUSIONS

The present study presents an analytical framework on double wedge failure plane of GRS wall and elaborates on site-specific PBD charts and reinforcement strength demand curve subjected to seismic loading. The effect of static and dynamic surcharge (q_t & $\alpha.q_t$) due to HSR passages on PBD charts considering various range of essential parameters of GRS walls (ϕ', γ, T_{ULT}, s_v, L/H, H) is also analyzed and compared against already published studies. A set of coefficients for varying range of L/H and critical yield acceleration ratios is presented for different scenarios to calculate the permanent displacement. A comprehensive design procedure implementing the current analytical framework is also discussed here. The key conclusions drawn from this study are summarized below:

i. Initial concave decremental curve highlights a non-linear relationship between geogrid reinforcement demand and seismic stability at low reinforcement levels ($k_t/\gamma H$ <1.8).
ii. Steep reinforcement demand (2.8< $k_t/\gamma H$ <5) at higher $k_{hy,c}^{int"}$ (0.25-1) with L/H=0.5 & ϕ'=32°, represents a transition from a compound failure to a steeper localized failure mode.
iii. Even at low L/H, higher soil shear strength (ϕ'=35°, 38°) provides sufficient stability to maintain gradual progression towards failure (3.5< $k_t/\gamma.H$ <6.5).
iv. Flatter & wider failure mechanism with reduced rate of increase in reinforcement demand (13.6%-16.7%) is observed for wall geometry $L/H \geq 0.7$.
v. Current approach may underestimate (27-96%) the true seismic capacity of GRS walls at high acceleration levels (0.5-0.8) due to consideration of higher a_{max} while disregarding plastic mechanism.
vi. Sudden shift of d_{perm} at about 0.34 for L/H<0.7, indicates ineffective reinforcements during transition of compound failure to localized steeper failure. Such behaviour is the reason behind the requirement of minimum L/H= 0.7 for GRS walls to avoid failure mechanism shift, coherent with internal guidelines.
vii. Dynamic surcharge amplified almost 1.6-6 times the effect of seismic loading than static and no surcharge, highlighting the necessity of accounting for PBD of GRS wall subjected to HSR passage.

7 ACKNOWLEDGEMENTS

The authors wish to thank the High-Performance Computing (HPC) facility of IIT Delhi & National Technical Textiles Mission, Ministry of Textiles, Govt. of India (NTTM) for generously funding the research project on the PBD of GRS walls for HSR and seismic loading (Sanction No. 2/8/2023-NTTM/ Project No. RP04661G).

8 REFERENCES

Bathurst, R. J. & Hatami, K., 1998. Seismic Response Analysis of a Geosynthetic-Reinforced Soil Retaining Wall. *Geosynthetics International,* 5(1-2), pp. 127-166.

Berg, R. R., Samtani, N. C. & Christopher, B. R., 2009. *Design and Construction of Mechanically Stabilized Earth Walls and Reinforced Soil Slopes-Volume I,* s.l.: Federal High Way Administration (FHWA).

BS 8006, 2010. *Code of Practice for strengthened/reinforced soils and other fills,* London, UK: British Standards Institution.

Cai, Z. & Bathurst, R. J., 1996. Seismic-induced permanent displacement of geosynthetic reinforced segmental retaining walls. *Canadian Geotechnical Journal,* 33(6), pp. 937-955.

Gaudio, D., Masini, L. & Rampello, S., 2018. A performance-based approach to design reinforced-earth retaining walls. *Geotextiles and Geomembranes,* 46(4), pp. 470-485.

Hatami, K. & Bathurst, R. J., 2006. Numerical Model for Reinforced Soil Segmental Walls under Surcharge Loading. *Journal of Geotechnical and Geoenvironmental Engineering,* 132(6), pp. 673-684.

Helwany, M. B., Tatsuoka, F., Tateyama, M. & Kojima, K., 1996. Effects of Facing Rigidity on the Performance of Geosynthetic-Reinforced Soil Retaining Walls. *Soils and Foundations,* 36(1), pp. 27-38.

Horii, K., Kishida, H., Tateyama, M. & Tatsuoka, F., 1994. *Computerized Design Method for Geosynthetic-Reinforced Soil Retaining Walls for Railway Embankments.* s.l., Recent Case Histories of Permanent Geosynthetic-Reinforced Soil Retaining Walls.

IRC: SP: 102, 2014. *Guidelines for design and construction of reinforced soil walls,* s.l.: Indian Roads Congress.

IS 18591, 2024. *Geosynthetic reinforced soil structures- code of practice,* India: Bureau of Indian Standards.

Jadhav, P. & Prashant, A., 2019. Recent Case Histories of Permanent Geosynthetic-Reinforced Soil Retaining Walls. *Soil Dynamics and Earthquake Engineering,* Volume 116, pp. 570-579.

Joseph, M. & Banerjee, S., 2025. Dynamic Performance Assessment of MSE Walls under High-Speed Train Loads. *International Journal of Geomechanics,* 25(2).

Kamalzadeh, A. & Pender, M. J., 2023. Dynamic response of Mechanically Stabilised Earth (MSE) structures: A numerical study. *Geotextiles and Geomembranes,* 51(1), pp. 73-87.

Koseki, J. et al., 1998. Shaking and Tilt Table Tests of Geosynthetic-Reinforced Soil and Conventional-Type Retaining Walls. *Geosynthetics International,* 5(1-2), pp. 73-96.

Kramer, S. L., 1996. *Geotechnical Earthquake Engineering.* s.l.:Prentice Hall.

Michalowski, R. L., 1997. Stability of Uniformly Reinforced Slopes. *Journal of Geotechnical and Geoenvironmental Engineering,* 123(6), pp. 546-556.

Newmark, N. M., 1965. Effects of Earthquakes on Dams and Embankments. *Géotechnique,* 15(2), pp. 139-160.

Prause, R., 1974. *Assessment of Design Tools and Criteria for Urban Rail Track Structures: Volume I. At-Grade Tie-Ballast Track, UMTA Report No. UMTA-MA-06-0025-74-4,* Springfield, Virginia: National Technical Information Service.

Rampello, S., Callisto, L. & Fargnoli, P., 2010. Evaluation of Slope Performance under Earthquake Loading Conditions. *Rivista Italiana di Geotecnica,* 44(4), pp. 29-41.

Richards, R. & Elms, D., 1979. Seismic Behavior of Gravity Retaining Walls. *Journal of the Geotechnical Engineering Division,* 105(4), pp. 449-464.

Siddharthan, R. V. et al., 2004. Seismic Deformation of Bar Mat Mechanically Stabilized Earth Walls. I: Centrifuge Tests. *Journal of Geotechnical and Geoenvironmental Engineering,* 130(1), pp. 14-25.

Sravanam, S. M., Balunaini, U. & Madhav, M. R., 2019. Behavior and Design of Back-to-Back Walls Considering Compaction and Surcharge Loads. *International Journal of Geosynthetics and Ground Engineering,* 5(4), p. 31.

Tatsuoka, F., 2021. *Manual for the design and construction of RRR Geosynthetic-Reinforced Soil structures,* Tokyo: ASSOCIATION OF RRR CONSTRUCTION SYSTEM.

Whitman, R. V. & Liao, S., 1985. *Seismic design of gravity retaining walls,* s.l.: No. WESMPGL851.

Woodruff, R., 2003. *Centrifuge Modeling of MSE-Shoring Composite Walls.* s.l.:Doctoral dissertation, University of Colorado.

Yazdandoust, M., Samee, A. & Ghalandarzadeh, A., 2023. Lateral Earth Pressure Distribution and Shear Band Development within Back-to-Back Mechanically Stabilized Earth Walls Under Seismic Conditions. *International Journal of Geomechanics,* 23(1).